Nanoscale Research Letters

NANO EXPRESS

Open Access

Nitrogen and Carbon Nitride-Doped TiO_2 for Multiple Catalysis and Its Antimicrobial Activity

Atif Ashfaq[1], Muhammad Ikram[1*], Ali Haider[2], Anwar Ul-Hamid[3*], Iram Shahzadi[4] and Junaid Haider[5]

Abstract

Nitrogen (N) and carbon nitride (C_3N_4)-doped TiO_2 nanostructures were prepared using co-precipitation route. Fixed amount of N and various concentrations (0.1, 0.2, 0.3 wt%) of C_3N_4 were doped in TiO_2 lattice. Through multiple techniques, structural, chemical, optical and morphological properties of samples were thoroughly investigated. XRD results verified anatase TiO_2 presence along the substitutional doping of N, while higher degree of crystallinity as well as increased crystallite size were noticed after doping. HR-TEM study revealed formation of nanostructures incorporated on two dimensional (2D) C_3N_4 nanosheet surface. Elemental composition was checked out using EDS technique which confirmed the presence of dopant in product. Optical characteristics were evaluated with UV–vis spectroscopy which depicted representative redshift in absorption spectra resulted in a reduction in bandgap energy in N/C_3N_4-doped TiO_2 samples. The formation of Ti–O–Ti bonds and different molecular vibrations were disclosed by FTIR. Trap sites and charge carrier's migration in the materials were evaluated with PL spectroscopy. Multiple catalytic activities (photo, sono and photo-sono) were undertaken to evaluate the dye degradation performance of prepared specimen against methylene blue and ciprofloxacin. Further, antimicrobial activity was analyzed against *Escherichia coli* (*E. coli*) and *Staphylococcus aureus* (*S. aureus*) bacteria.

Keywords: Co-precipitation, Photocatalysis, Sonocatalysis, Dye degradation, Methylene blue

Introduction

In the past few years, researchers and scientists have paid greater attention to energy crisis and environmental and aquatic pollution. In today's technology driven society, relentless consumption of fossil fuels is serving to make these issues worse [1]. Fossil fuels, the rich energy-generation source, are contracting worldwide and developed countries are switching to sustainable and environment-friendly technologies. On the other hand, textile industry produces wastewater containing 5–15% of untreated organic dyes. Around 1×10^5 dyes are in use globally and 7×10^5 ton dyestuff is generated by the textile industry worldwide annually. Discharge of these untreated dyes not only affects the oxygen and nitrogen cycle connected to photosynthesis but also causes grave esthetic deterioration [2]. These are some of the serious environmental issues that need to be addressed to sustain human society in the long term.

Properties of bulk materials depend a lot on size and structure [3]. In this regard, nano-scaled semiconductors with diverse properties are used for photocatalytic and dye degradation applications [4]. Various transition metals (TMs) Ti, Cu, Fe, Co and non-metals (NMs) N, C, S etc., exhibit distinct physical and chemical properties [5]. In this regard, a combination of TM (titanium–dioxide) and NM (nitrogen) exhibit additive properties. Combination of semiconductors (with metals and metal oxides) that bear appropriate band arrangements possess striking

*Correspondence: dr.muhammadikram@gcu.edu.pk; anwar@kfupm.edu.sa
[1] Solar Cell Application Research Lab, Department of Physics, Government College University Lahore, Lahore, Punjab 54000, Pakistan
[3] Core Research Facilities, King Fahd University of Petroleum and Minerals, Dhahran 31261, Saudi Arabia
Full list of author information is available at the end of the article

applications in energy production and water treatment [6]. Rare earth metals oxides such as TiO_2, CdO, CoO, ZnO, etc., are leading candidates for many such applications. Amongst these, TiO_2 holds limited activity in visible region due to its high band gap value (3.0 eV for rutile phase, 3.2 eV for anatase phase) [7], low surface area and high electron–hole recombination [8]. In 1972, TiO_2 was used for the decomposition of water using UV light [9]. Since then, photocatalysis with semiconductors has gained much attention due to their potential applications such as in hydrogen production and environmental cleaning [10]. Semiconductors with unique band gap (occupied valence band and unoccupied conduction band) serve as suitable catalysts for photochemical reactions. Currently, the main focus is visible light region through band gap tuning of inorganic semiconductor.

TiO_2 is a semiconductor with prominent features including tunable band gap, simple synthesis routes and ecological-friendly nature. Therefore, to improve the photocatalytic activity of TiO_2 nanostructures, modulation of its band gap was undertaken by adding nitrogen (N) for better absorption of solar spectrum. N was added through CH_4N_2O source which contains 46% of its concentration [7, 11]. As a result, bandgap of TiO_2 varied from 3.2 to 3.06 eV (substitutional replacement of N with oxygen) or it can also be varied from 3.2 to 2.46 eV (interstitial doping) which is more preferable for visible light [12–14]. Dopant C_3N_4 is a 2D material which resolves the impediment of low surface area of TiO_2 to enhance photocatalytic activity upon addition in various concentrations and exhibit broader spectral response near the visible region compared to pristine TiO_2. Moreover, C_3N_4 has promising applications due to a suitable band gap (2.7 eV) which has the ability to enhance photocatalytic activity of TiO_2 for use in dye degradation [15–18].

TiO_2 nanostructures can also be utilized as antibacterial agent. The antibacterial activity of TiO_2 nanostructures is assigned to reactive oxygen species (ROS) such as hydroxyl radicals and hydrogen peroxide, which induce severe oxidative stress on bacterial strain generated under illumination. Therefore, TiO_2 is a potential candidate for antibacterial agent. The generated ROS provide a contact between TiO_2 and cells which kills the cell due to damage aroused in DNA and cell membrane that ultimately results in termination of cell cycle [19]. The antimicrobial activity of prepared antibiotic also depends on surface area, morphology, crystallinity, concentration/dosage, pH of the solution, capping agent, and also the nature of microorganisms. Combining the merits of C_3N_4 with TiO_2 and N, prepared composite is important to solve the problems of the environmental crisis in worldwide including organic water pollutants and pathogenic microbial contaminations [20, 21]. Few studies have been reported for the antibacterial activity and degradation of different dyes [5, 8, 11], best of our knowledge, this novel study report the efficiency of C_3N_4-doped N/TiO_2 nanocomposites synthesized by co-precipitation route.

In this paper, co-precipitation method was used to synthesize pristine and doped TiO_2 nanostructures. This study revealed the strong contact formation of TiO_2 with dopants (N and C_3N_4) which efficiently increased the photocatalytic activities against methylene blue and ciprofloxacin as well as antibacterial property against *E. coli* and *S. aureus* bacteria.

Experimental Details

Materials

Urea (CH_4N_2O) (99%) and titanium (IV) butoxide ($Ti(C_4H_9O)_4$) (98%) were received from Sigma-Aldrich, Germany while ethanol (C_2H_5OH) (95%) was purchased from Panreac. Carbon nitride (C_3N_4) was obtained from pyrolysis of CH_4N_2O in the laboratory (Fig. 1a). All the reagents were used without further purification.

Preparation of TiO_2 Nanostructures

Titanium-dioxide (TiO_2) was prepared by adopting co-precipitation method where 55 mL of ethanol, 13 mL of $Ti(C_4H_9O)_4$ and 5 mL of deionized water (DI water) were mixed and stirred vigorously for 30 min. Ethanol (~ 100 mL) and DIW (~ 100 mL) were added to the stirred solution for 2 h at 50 °C. The pH of solution was maintained up to ~ 10 using NaOH (0.5 M) solution. Then, solution was centrifuged and dried at 90 °C for 10 h. After that, sample was annealed at 450 °C for 4 h to achieve stable anatase nanostructures (Fig. 1b).

Preparation of C_3N_4Doped N-TiO_2

Various concentrations (0.1, 0.2, 0.3 wt%) of C_3N_4 was doped into N-TiO_2 mixture. $Ti(C_4H_9O)_4$ (17.45 mL), CH_4N_2O (3 g), C_2H_5OH and DI water were added under vigorous stirring. Samples were sonicated for homogenous mixing. Sonicated samples were centrifuged at 4000 rpm and dried at 90 °C for 10 h and annealed at 450 °C for 4 h to obtain stable nanostructures. Six samples were prepared and named as TiO_2, nitrogen-doped TiO_2 (N-TiO_2 as 0:1), pristine carbon nitride (C_3N_4 1:0) and different concentrations of C_3N_4 in N-TiO_2 named as 0.1:1, 0.2:1, 0.3:1.

Evaluation of Photocatalytic Activity

The photocatalytic activity (PCA) of synthesized catalysts was assessed by estimating the degradation rate of a combination of two toxic dyes namely methylene blue (MB) and ciprofloxacin (CF) in aqueous solution. The stock solution of dyes was prepared in DIW (10 mg/1000 mL) and 10 mg of prepared catalyst (pristine TiO_2, C_3N_4, 0:1,

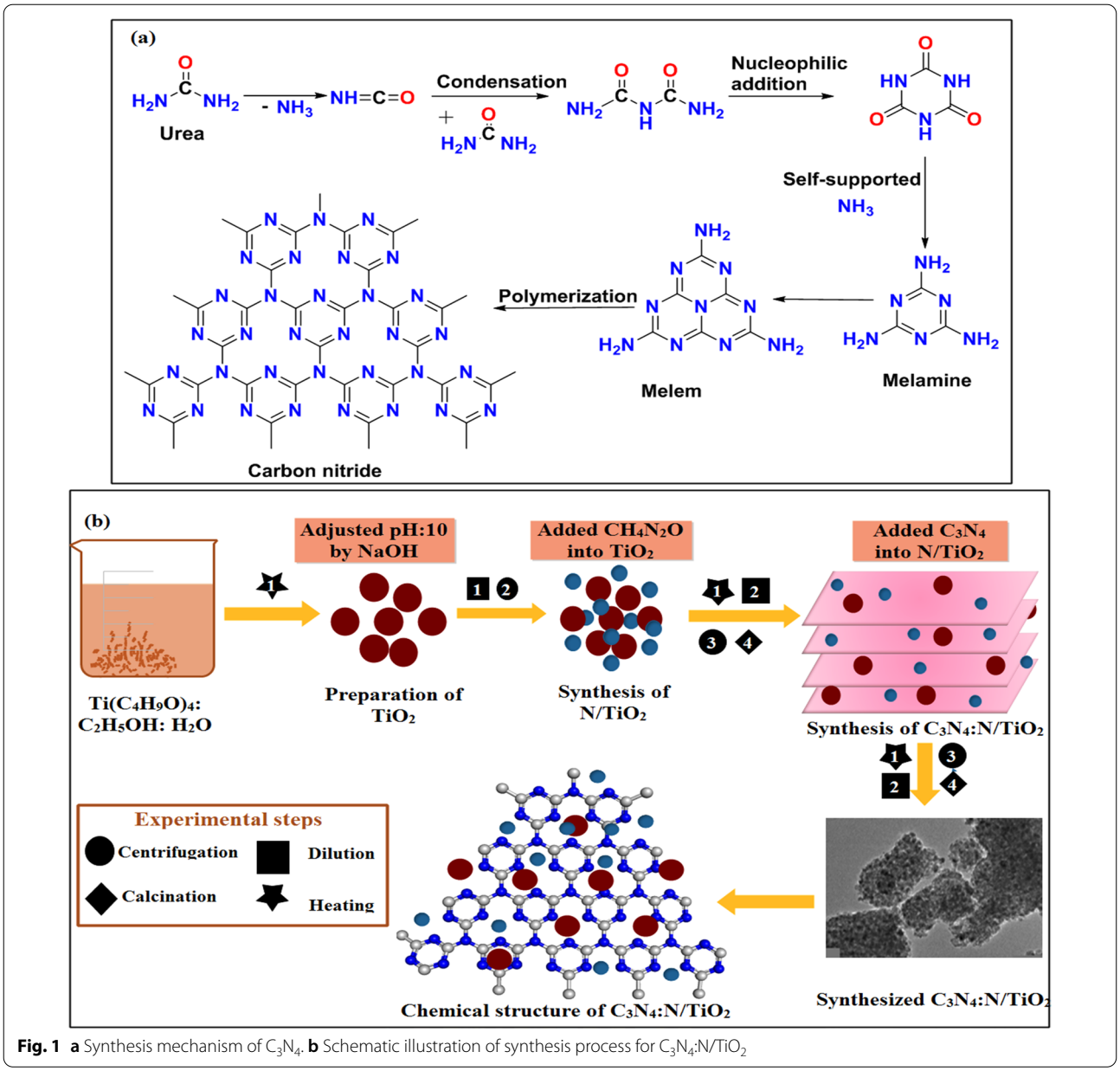

Fig. 1 **a** Synthesis mechanism of C_3N_4. **b** Schematic illustration of synthesis process for C_3N_4:N/TiO_2

0.1:1, 0.2:1, 0.3:1) was added to 50 mL stock solution. After homogeneous stirring, solution was placed in a sealed box under mercury (Hg) lamp (wavelength 400 to 700 nm and power 400 W) at ~ 15 cm distance to avoid overheating. After 20 min interval, 3 mL solution was separated to check concentration of dyes present in the solution by utilizing UV–Vis spectroscopy. The degradation efficiency was determined by the formula given as:

$$\text{Degradation efficiency}\,(\%) = \frac{Co - Ct}{Co} \times 100 \qquad (1)$$

where C_o and C_t initial and final concentration of dye at time $t = 0$ and at final time t, respectively [22].

2-Diphenyl-1-Picrylhydrazyl (DPPH) Radical Scavenging Assay

Free radical scavenging activity of all samples was examined using the method reported by Kibiti and Afolayan [23] with certain modifications. Various concentrations of pristine TiO_2, C_3N_4, and C_3N_4 doped TiO_2 nanoparticles (0–500 µg/mL) were prepared and mixed with equal volume of 0.1 mM DPPH solution. The reaction mixture was vortex and incubated for 30 min in dark at ambient

temperature. Ascorbic acid was employed as a reference antioxidant. Absorbance of mixture was measured at 517 nm using spectrophotometer. The % scavenging ability was calculated using equation:

$$\text{DPPH scavenging rate}(\%) = \frac{(A_0 - A_1)}{A_0} \times 100$$

where A_0 is absorption of control (Methanol + DPPH) and A_1 is absorbance of sample.

Bacterial Segregation and Identification

With ovine mastitic milk specimen's antibacterial evaluation was undertaken on *S. aureus* and *E. coli* isolated after initial screening at ovine blood agar (5%) and finally on mannitol salt agar (MSA) and MacConkey agar (MCA), respectively. Coagulase, catalase, and Gram' staining protocols were used to classify extracted commodities (biochemically and morphologically).

Antimicrobial Activity

Well diffusion procedure was adapted to assess antibacterial effects of N and C_3N_4 co-doped TiO_2 by swabbing 1.5×10^8 CFU mL^{-1} of purified bacterial isolates on MCA and MSA, separately. On swabbed dishes, 6 mm deep wells were drilled with aseptic well borer. Various dilutions of doped nanomaterial's e.g., 500 and 1000 µg/50 µL were placed into wells as minimum and maximum dosage in contrast with ciprofloxacin as positive control (5 µg/50 µL) and DIW (50 µL) as negative control. The sensitivity of all prepared samples was measured with a Vernier caliper after overnight incubation (37 °C) of Petri plates. Antibacterial evaluation was contemplated by utilizing one-way analysis of variance [24].

Material Characterization

Phase transition and crystal structure of binary-doped TiO_2 was examined with XRD utilizing spectrum Bruker system with monochromatic Cu K-α ($\lambda = 0.154$ nm and $2\theta = 10°–80°$) with a scan rate of 0.05° per minute. The study of functional groups and chemical analysis was undertaken utilizing FTIR spectrometer (PerkinElmer 3100) with range of spectra from 4000 to 400 cm^{-1} in 32 scans and a resolution of 0.2 cm^{-1}. The optical study was carried out with Genesys 10S spectrophotometer (ranging from 200 to 800 nm). Interlayer spacing and surface morphology of prepared products were inspected through HR-TEM and EDS spectrometer, JSM-6460LV, and HRTEM Philips CM30 and JEOL JEM 2100F. Photoluminescence spectroscopy was carried out to inquire transfer and recombination of e^- to h^+ pairs utilizing a spectrofluorometer (JASCO, FP-8300).

Results and Discussion

To analyze the structure of the crystal, phase purity and size of crystallites, XRD was employed on control and N/C_3N_4-doped TiO_2 in 2θ range of 10°–80° (Fig. 2a). Acquired spectra revealed peaks at 25.4°, 37.8°, 48.1°, 53.9°, 55.1°, 62.7°, 68.6, 70.3° and 75.1° attributed to (101), (004), (200), (105), (211), (204), (116), (220), (215) planes of tetragonal anatase formation, respectively (JCPDS no. 21-1272). For N-TiO_2 composite, no significant change in XRD spectrum was observed which might be referred to relatively lower concentration of N in the composite. Hexagonal structure for C_3N_4 was confirmed from peaks generated at 13.2° (100) and 27.4° (002) reflecting the standard spectrum (JCPDS no. 87–1526). No shift in peaks was observed upon doping for 0.1:1 (lower) and 0.2:1 (intermediate) and 0.3:1 (higher) concentration samples, however the sharpness in peaks indicated the successful coupling of C_3N_4:N/TiO_2, resulting in enhanced crystallinity and structural quality [25, 26]. The interlayer spacing of pristine TiO_2 (~0.352 nm) and N-TiO_2 (~0.35 nm) were calculated from the most intense peak (101) using Debye-Scherer formula which were further verified by HR-TEM observation.

SAED (Selected Area Electron Diffraction) profiles of pristine TiO_2, 0:1 (N-TiO_2) and 0.1:1 sample are given in Fig. 2b–d. Images were indexed with diffraction planes (004), (101), (105), (116), (200), (204), (211) confirmed by XRD results, showing the tetragonal crystal structure of TiO_2.

Various functional groups and chemical compositions present in as prepared samples were identified using FTIR analysis (Fig. 2e). In acquired spectra, it can be seen that absorption band stationed at 400–700 cm^{-1} corresponds to Ti–O and Ti–O–Ti stretching vibration modes, which indicated TiO_2 formation. This vibration band has been linked with physiosorbed water protons in synthesized samples [27–29]. Band observed at about 1635 and 3200–3500 cm^{-1} referred to hydroxyl (O–H) group and physically absorbed water on pristine TiO_2 surface, respectively [30, 31]. In C_3N_4 spectrum, absorption band at 1624 cm^{-1} was attributed to C-N heterocycle stretching vibrational modes [32], while four bands at 1232, 1304, 1411, 1556 cm^{-1} were referred to aromatic C–N stretching vibrational modes [33, 34]. Notably, all characteristic peaks of TiO_2 and C_3N_4 can be observed, validating the formation of C_3N_4:N/TiO_2 nanostructure.

The morphology and crystal structure of pristine TiO_2 (Fig. 3a), 0:1, 1:0, 0.1:1 and 0.3:1 nanostructure were studied by TEM analysis. Figure 3b represents N-TiO_2 composite with a high surface energy that leads to aggregation [35] and Fig. 3c is the illustration of C_3N_4,

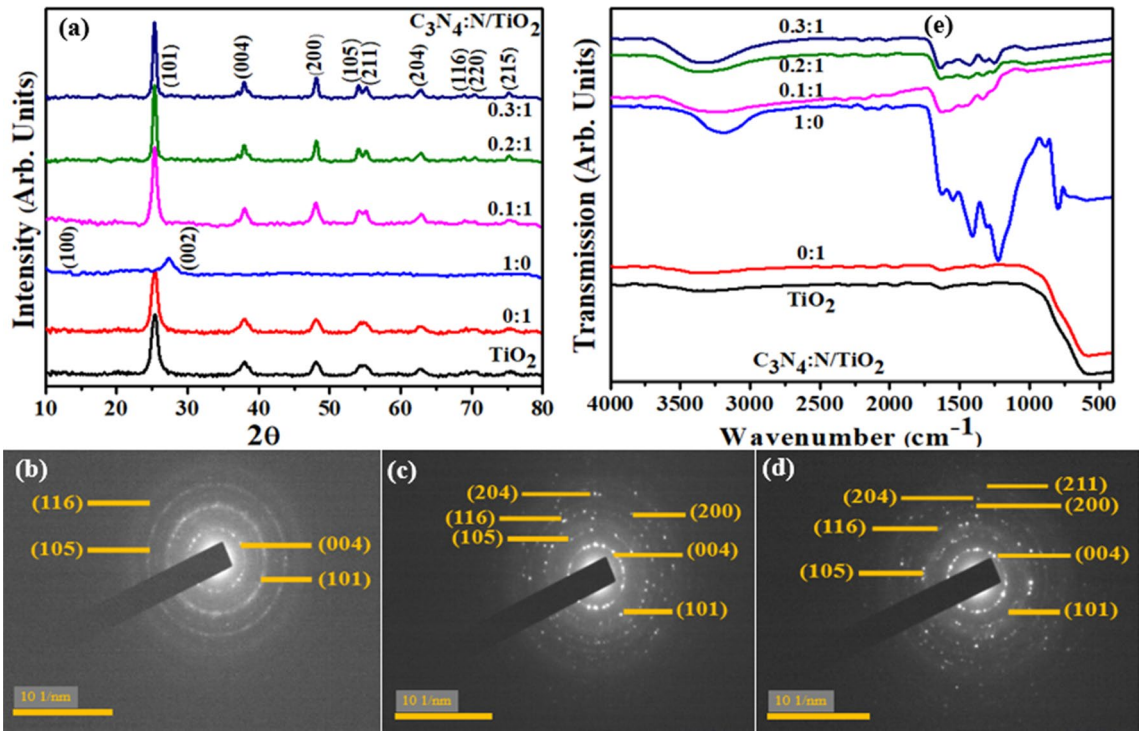

Fig. 2 **a** XRD pattern. **b** FTIR spectra. **c**–**e** SAED profiles of as-synthesized co-doped TiO_2. **c** TiO_2. **d** 0:1. **e** 0.1:1

a mesoporous nanosheet (NS). Upon C_3N_4 addition, N-TiO_2 composite was embedded and well distributed on NS which also roughly confirmed the C_3N_4 wrapping, as illustrated in Fig. 3d. This intimate interfacial contact between N-TiO_2 composite and NS was necessary for photocatalytic activity. Upon doping, crystallinity of prepared nanostructures improved and after higher doping, NS wrapped N-TiO_2 composite and ultimately made an efficient interfacial contact (Fig. 3e). In HR-TEM image of 0.1:1 (Fig. 3c′), interlayer spacing was calculated to be 0.35 and 0.33 nm pertaining to (101) and (002) crystal planes of N-TiO_2 composite and C_3N_4, respectively, in consistence with XRD results. Interlayer spacing has been measured for each sample using Gatan software, given in Fig. 3á–đ.

In order to check further interfacial contact, EDX mapping of as-prepared C_3N_4 (1:0) and 0.3:1 (higher doping) samples was conducted to inspect distribution pattern of its components. As revealed in Fig. 4a, five components (C, N, Ti, O, Na) were found to be uniformly dispersed in higher doped specimen. Sodium (Na) came from sodium hydroxide (NaOH) added for maintaining pH of solution up to ~ 10. Combined with HR-TEM and XRD results, it recommended that within 0.3:1 sample, N and TiO_2 nanoparticles are certainly well dispersed inside wrapped C_3N_4 NS and indicated intimate contact as well.

Elemental composition was evaluated by EDX to confirm the purity of 0.3:1 (higher doping) and 1:0 (Fig. 4b–c). As illustrated in Fig. 4b, Ti indicated peaks at 4.5 and 4.95 keV, oxygen (O) peak at 0.5 keV, C and N peaks at 0.3 and 0.4 keV, along with several other positions were detected, confirming successful incorporation of binary-dopant species with anatase TiO_2.

To determine optical performance of undoped and doped TiO_2, UV–vis spectroscopy was used in the range 300–550 nm. TiO_2 has characteristic absorbance peak found around ~ 350 nm, with N-doping, slight redshift was observed in absorption spectra caused by overlapping of 2*p* orbitals of O_2 and N, as shown in Fig. 5a [36]. An increase in spectral absorbance was observed upon C_3N_4 doping into N-TiO_2 composite, attributed to complete planarization of C_3N_4 (non-overlapping of adjacent orbitals). Enhanced absorptive ability in UV-region was assigned to internal scattering and harmonious effect from N-TiO_2 and C_3N_4's π to π^* and n to π^* transitions, respectively, as depicted in Fig. 5b [37]. Peaks redshifted due to molecular engineering of C_3N_4 in N-TiO_2 composite that potentially advanced absorption and transition ability of charge carriers [38]. Tuac transformation was applied to calculate bandgaps of prepared samples. For TiO_2 bandgap was calculated to be 3.2 eV and gradual decrease in bandgap energies were observed close to

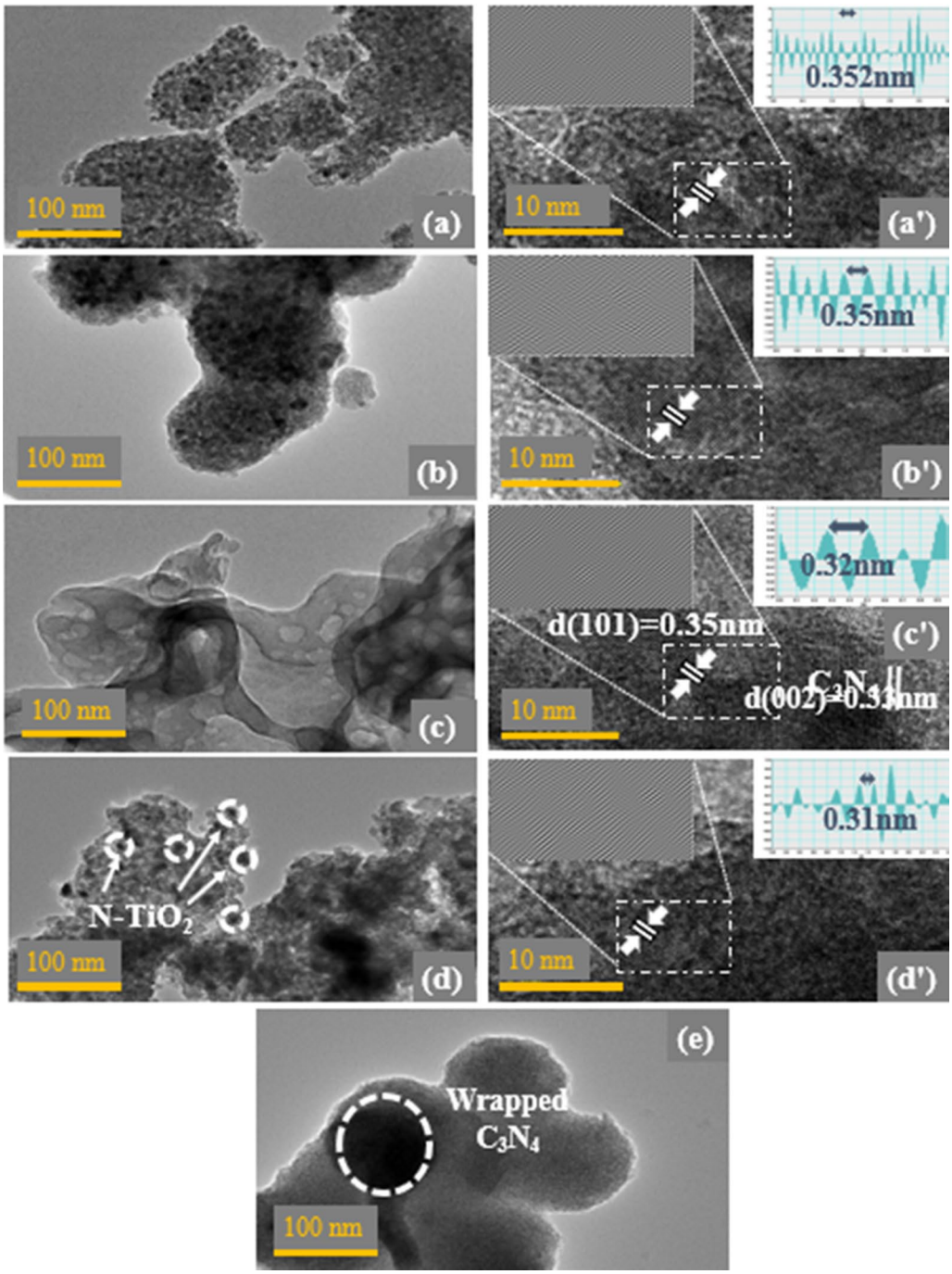

Fig. 3 **a**–**e** HR-TEM micrographs of pristine TiO_2, 0:1, 1:0, 0.1:1, 0.3:1, respectively. **a′**–**d′** Interlayer spacing measured using HR-TEM images of pristine TiO_2, 0:1, 0.1:1, 0.3:1, respectively

Fermi level after adding N and C_3N_4 to ~ 2.9 eV, as given in Fig. 5c–h [39].

PL emission spectra of TiO_2 and its composites were computed from 410 to 520 nm with an excited wavelength of 350 nm at room temperature, as illustrated in Fig. 6a. Spectra unveiled migration and electron–hole (e^- to h^+) pairs recombination efficiency [40]. Characteristic peak of TiO_2 at 455 nm showed the highest recombination of e^- to h^+ pairs which significantly limited PCA of TiO_2 whereas recombination rate was decreased upon

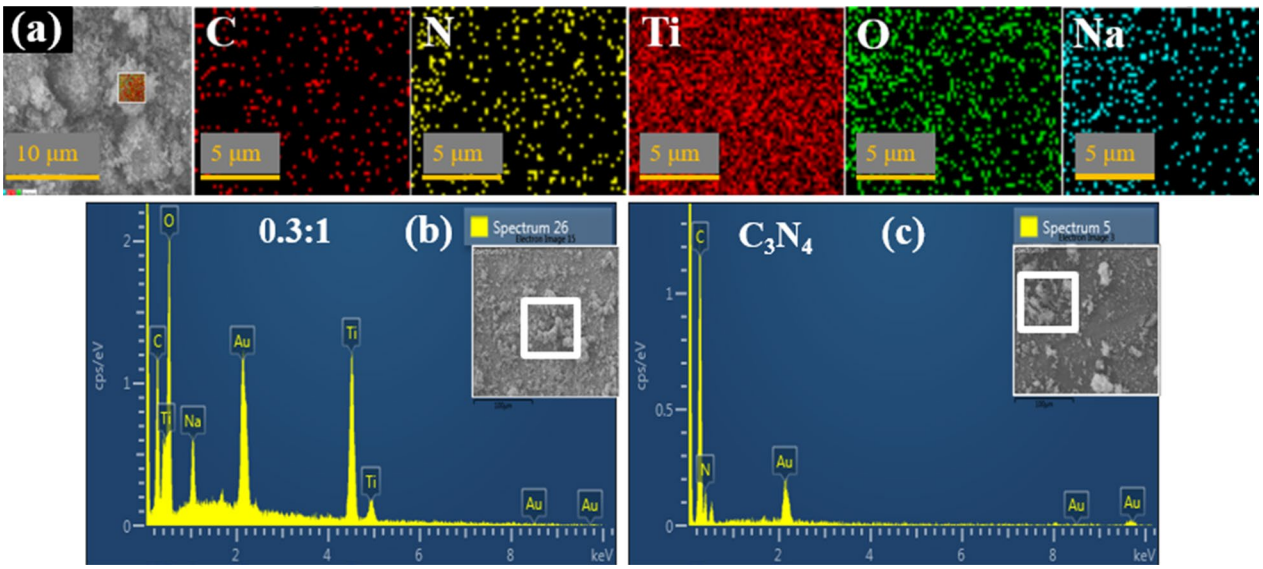

Fig. 4 **a** Mapping of 0.3:1 sample to ensure distribution of all components (**b**–**c**) EDX images of 0.3:1 (higher doping) and 1:0, respectively

co-doping (N and C_3N_4). Shockley–Read–Hall (SRH) process explains bandgap transitions from valence band to sub-band and then to conduction band [41]. Sub-band at the edge of conduction band facilitated PCA [42], so for higher doping sample, lower recombination rate proposed higher photo-generated charge transportation that internally enhanced PCA of 0.3:1.

Reaction Mechanism and Kinetics

The following mechanism was involved in PCA of prepared catalyst (see Fig. 7):

1. Photoexcitation: The PCA first involves photoexcitation that initiates by the photons processing equal or greater energy than bandgap energy (E_g) of material. These photons stimulate electrons of valence/lower band (VB) and migrate them to conduction/higher band (CB). Electrons leave holes behind in VB resulting in e^--h^+ pairs generation, as shown in equation below.

$$TiO_2 + h\nu \rightarrow TiO_2\left(e^-\right) + h^+ \tag{2}$$

2. Ionization of water: Holes create $OH^\bullet$ free radicals after coming into contact with water (H_2O).

$$H_2O + h^+ \rightarrow OH^\cdot + H^+ \tag{3}$$

The $OH^\bullet$ radical act as an oxidizing agent on the surface of semiconductor that targets adsorbed molecules and takes part in mineralization.

3. Oxygen ionosorption: Photogenerated es^- comes into contact with water molecules and generate OH^- (hydroxyl group) while es^- are trapped by molecules of O_2 to produce $O_2^{\bullet-}$ (superoxide radical) [43].

$$O_2 + e^- \rightarrow O_2^{\cdot-} \tag{4}$$

The superoxide radical contributes in oxidation cycles and inhibits the recombination of e^- and h^+ while keeping the TiO_2 neutral.

4. Superoxide protonation: Superoxide ions (O_2^-) gives $H_2O^\bullet$ (protonated hydroperoxylate radical) and finally H_2O_2 generate $OH^\bullet$ radical that is highly reactive.

$$O_2^{\cdot-} + H \rightleftharpoons HOO^\cdot \tag{5}$$

$$2HOO^\cdot \rightarrow H_2O_2 + O_2 \tag{6}$$

$$H_2O_2 \rightarrow 2OH^\cdot \tag{7}$$

$$\text{Dye (MB and CF)} + OH^\cdot \rightarrow CO_2 + H_2O\left(\text{dye intermediates}\right) \tag{8}$$

$$\text{Dye} + h^+(\text{VB}) \rightarrow \text{oxidation products} \tag{9}$$

$$\text{Dye} + e^-(\text{CB}) \rightarrow \text{reduction products} \tag{10}$$

Oxidation/reduction reactions occurred on photo-excited photocatalysts surface [44, 45].

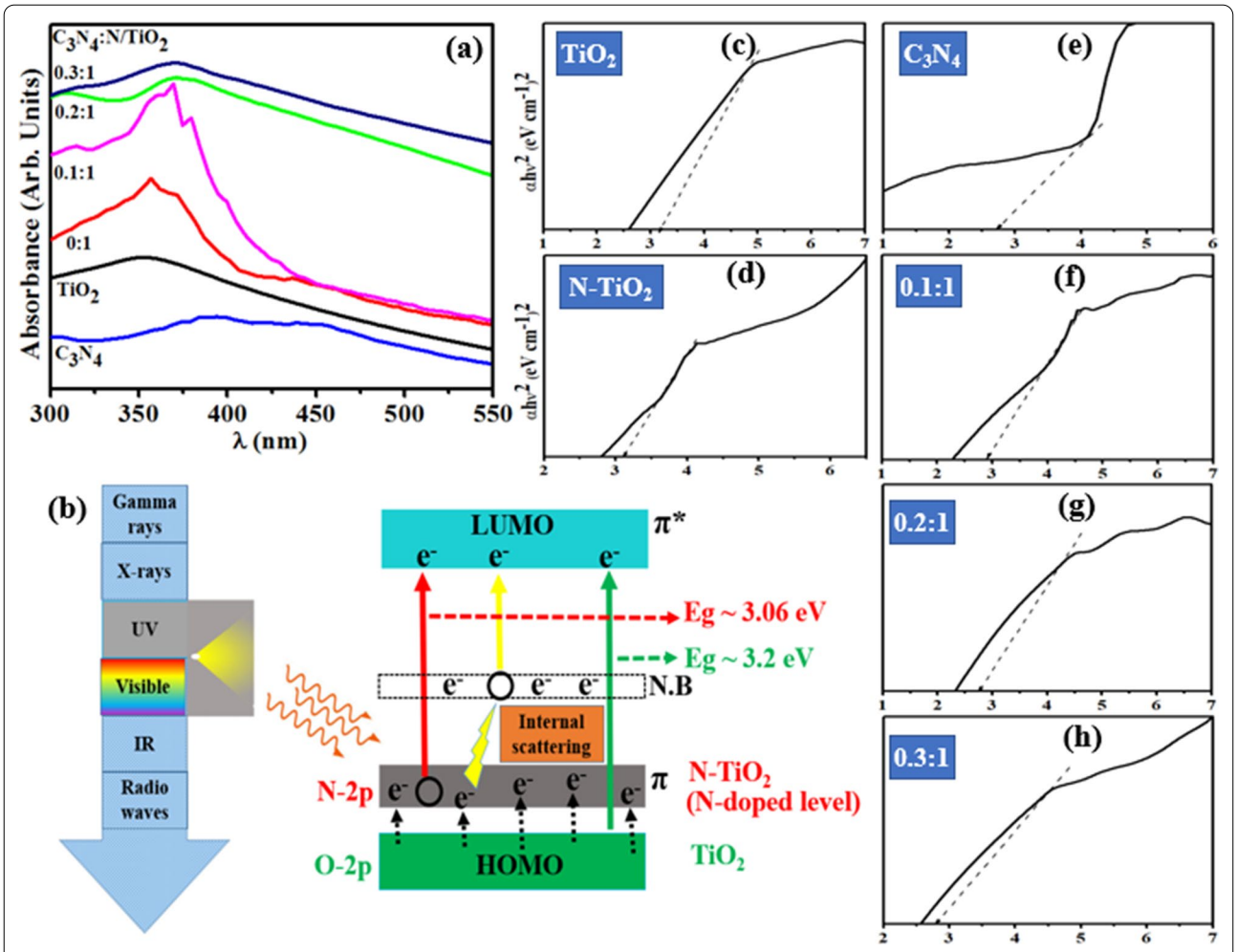

Fig. 5 **a** Optical absorbance spectra (**b**) possible transitions and internal scattering in UV-vis spectroscopy (**c**–**h**) determination of bandgap of TiO_2, N-TiO_2, C_3N_4, 0.1:1, 0.2:1 and 0.3:1, respectively

The PCA of as-prepared samples was evaluated for degradation of MB and CF dye under replicated visible light irradiation (Fig. 6b). The blank test demonstrated that MB and CF could not be degraded under irradiation of light in the absence of catalyst thus it can be deduced that MB and CF were stable. As indicated in Fig. 6c, C3N4 degraded the targeted dye up to 45% and enhanced photocatalytic activity of nanostructures was observed with increasing C_3N_4 concentration which effectively degraded MB and CF. In case of N-TiO_2, relatively higher extent of degradation (58%) occurred as compared to TiO_2 (32%) while highest doped sample (0.3:1) showed maximum degradation of 85% within 80 min. The apparent reaction rate constants (k) were determined for all specimens by measuring slopes of ln (C_o/C_t) against time plot. Moreover, k value of 0.3:1 was also higher than others, which was ~ 2.5 times higher than pristine TiO_2 (Fig. 6d).

The enhanced PCA of nanostructures may be attributed to these measures: firstly, the C_3N_4 sheet has a larger surface that encouraged broad adsorption within catalyst and furnished additional active sites for surrounding reactants. Secondly, after incorporation of N and C_3N_4 in TiO_2, increased charge separation efficiency by inducing new energy levels within the forbidden band gap of TiO_2. These induced levels act as trapping sites for photo induced electrons increasing the electron transfer efficiency which ultimately improved the degradation

performance of nano-catalysts. Thirdly, due to intimate and well-matched band edge, N-TiO_2 collects photo-induced electrons from the CB of C_3N_4 thus improving the charge separation efficiency. In general, C_3N_4 produces e^- to h^+ pairs under visible light that quickly recombine and only a small fraction of e^- participate in PCA. Whereas when TiO_2 was modified by binary dopants to form a nanocomposite, photo-generated electrons in CB of C_3N_4 can directly move to CB of N-TiO_2 composite, as shown in Fig. 7, because CB edge of C_3N_4 was more negative than N-TiO_2. The above-mentioned parameters eventually increased overall photocatalytic activity of as-prepared nano-composites [46–48].

Sonocatalytic activity (SCA) was also measured by degrading MB and CF via ultra-sonication route. Same as for PCA, samples were collected after 20 min interval in SCA. As illustrated in Fig. 8c, C3N4, TiO_2, N-TiO_2 composites degraded the MB and CF up to 36%, 20% and 27% in 80 min while for lower doping, activity of 0.1:1 nanostructure increased up to 60% and then decreased for further and higher doping concentrations. For lower doping, catalyst formed the microbubbles and bore more active sites for growth of nucleation, further generated more reactive radicals [49] and for further doping, active sites of prepared catalysts were insufficient to be occupied by dye molecules. Second possible reason could be surplus of C_3N_4 amount that have restricted the energy obtained from ultrasound wave [50].

The rate constants (k) have been calculated for sono-degradation kinetics by measuring slopes on ln (C_o/C_t) against time as shown in Fig. 8b. PCA and SCA of pristine TiO_2 and C_3N_4 were less efficient, thus N/C_3N_4-doped TiO_2 composite turned up as potential catalyst for dye degradation.

The combined effect of PCA and SCA has been evaluated further by adjusting sonometer under light source

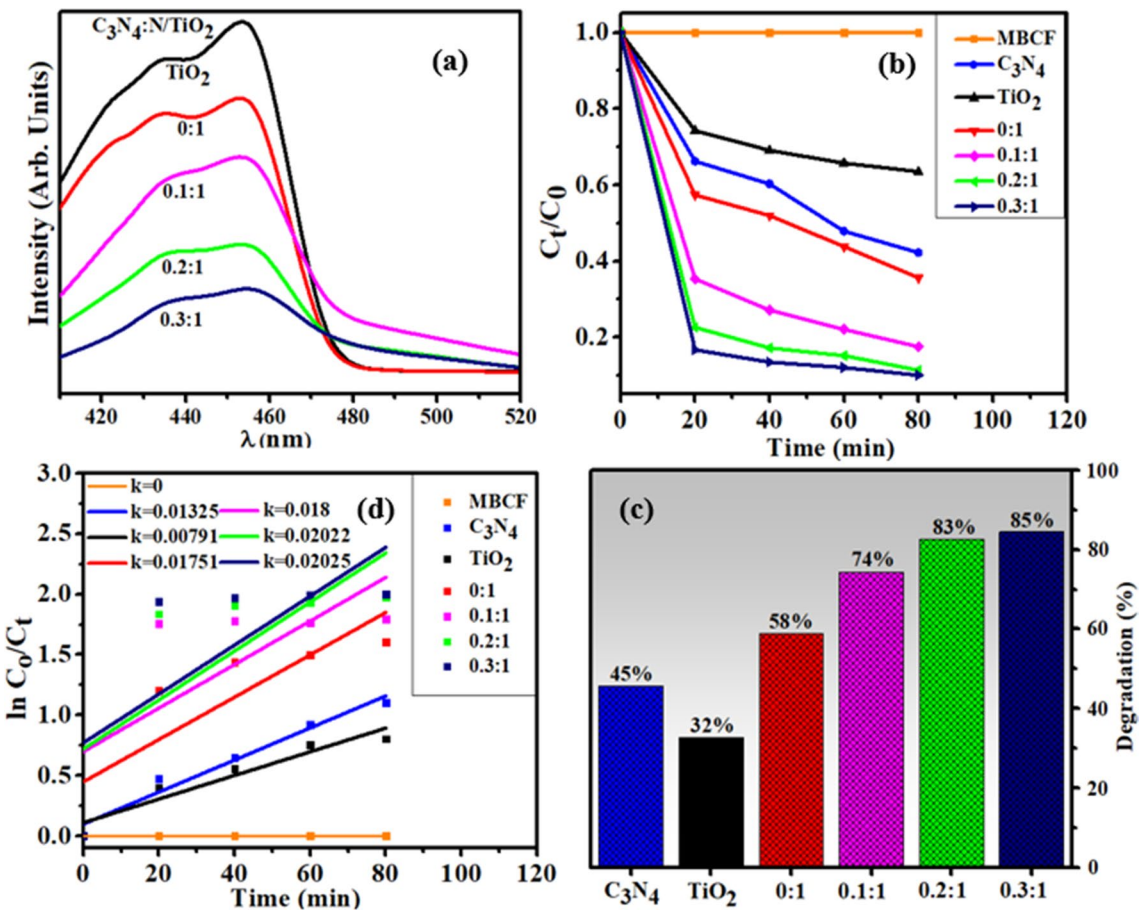

Fig. 6 **a** PL spectra (**b**) Plot of concentration ratio (C_t/C_o) versus time (**c**) percentage (%) degradation of all samples (**d**) plot of ln(C_o/C_t) versus time spectra for dye reduction

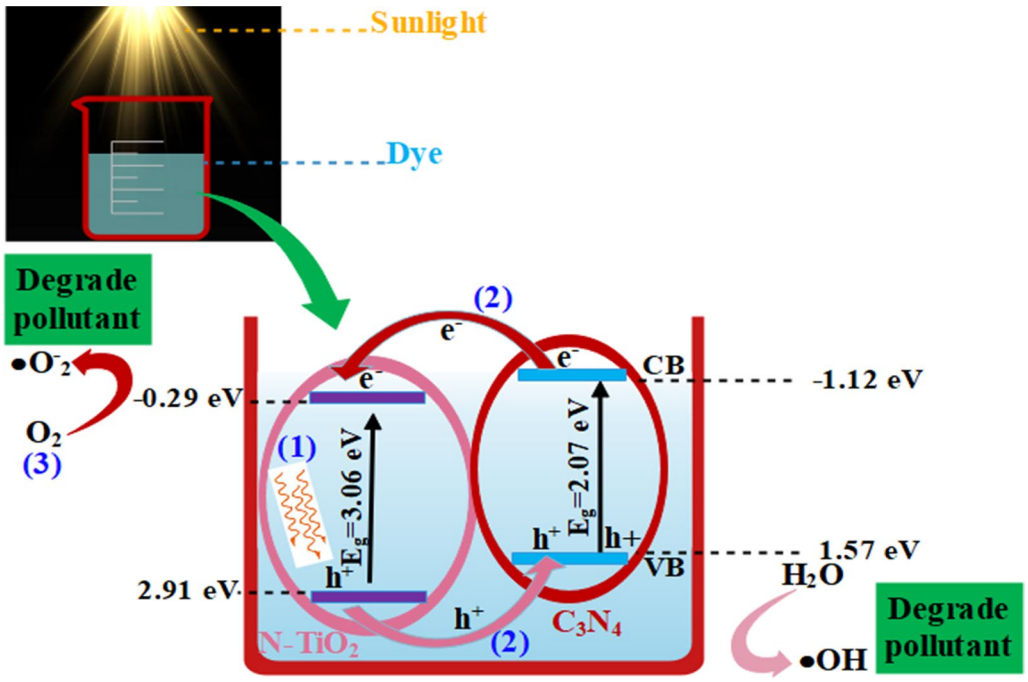

Fig. 7 Mechanism for degradation of dyes in the presence of prepared photocatalyst

for all synthesized samples. The earned results unveiled that pristine C_3N_4, TiO_2 and N-TiO_2 composite degraded dye up to 60%, 40% and 55%, respectively. For lower doping, 0.1:1 nanostructure degraded MB and CF up to 86% caused by combined effect of PCA and SCA. But for further and higher doping (although assisted by PCA) active sites were insufficient that might be ascribed to dominant effect of SCA that subsequently decreased the degradation performance. Also, surplus amount of C_3N_4 and inhomogeneous mixing of catalysts can cause agglomeration which might limit the energy obtained from ultrasound wave and visible light source (Fig. 9c).

For photo-sono degradation kinetics, the rate constants (k) have been estimated by computing slopes on ln (C_o/C_t) against time, as manifested in Fig. 9b.

Antioxidant characteristics of compounds is tied to their electron or hydrogen atom donating capability to DPPH free radical, such that they create stable diamagnetic compounds [51]. This DPPH free radical's reduction capability can be examined by lowering the absorbance at 517 nm.

All synthesized compounds were evaluated for antioxidant activity using a DPPH radical scavenging assay. Using ascorbic acid as a reference, DPPH disappearance was evaluated spectrophotometrically at 517 nm. In this study, it was discovered that the DPPH activity of the nanoparticles increased in a dose-dependent manner (Fig. 10). It is confirmed that Pristine TiO_2 showed high scavenging activity (50.22%) at concentration of 500 µg/mL compare to C_3N_4. Because TiO_2 may form $OH^{\cdot}$, $O_2^{\cdot -}$ and $^1O_2$ reactive oxygen species, which have the potential to bond with the DPPH free radical [51–53]. Some recent studies have reported $^1O_2$ to be the dominant active specie in the degradation of MB dye under solar irradiation [53, 54]. While N-TiO_2 showed DPPH scavenging up to 57.34% that is 7% higher than that of TiO_2. This considerable increase is resulted from the addition of a doping agent which lowers the size of TiO_2 nanoparticles and increases their reactivity [55, 56]. In case of C_3N_4 doped TiO2 with mass ratio of 0.1:1, scavenging activity increased up to 84.45% that might be the availability of sufficient amount of nitrogen from doped C_3N_4. But increasing the concentration of doped C_3N_4 on N-TiO_2, scavenging activity was decreased. This was due to high C_3N_4 concentration caused an increase in turbidity of test sample, which in turn caused an antagonistic interaction resulted in a decrease scavenging activity (84.45–70.75%) [50].

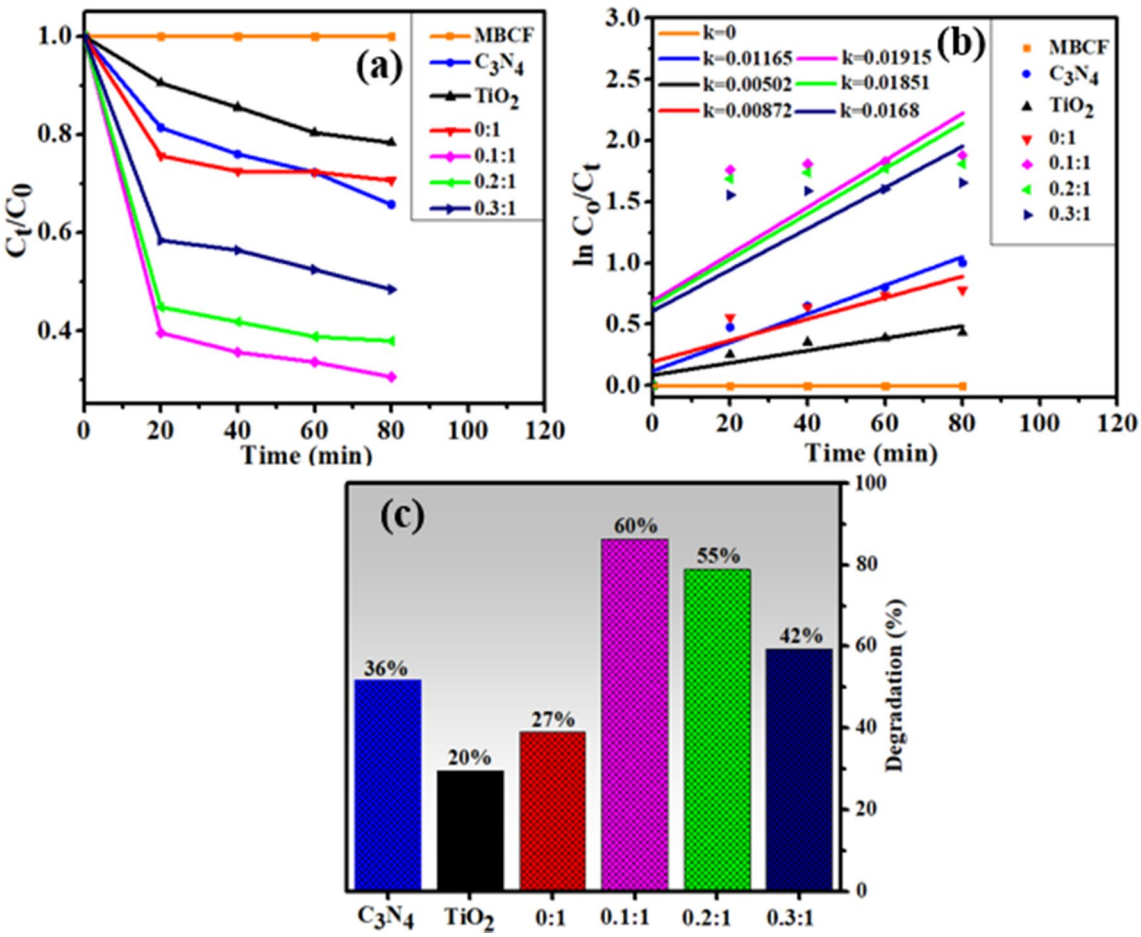

Fig. 8 **a** Plot of concentration ratio (C_t/C_o) versus time, **b** plot of ln(C_o/C_t) versus time spectra for dye reduction, **c** percentage (%) degradation of prepared specimens

Antimicrobial activity of binary doped TiO_2 was conducted using well diffusion technique (Fig. 11) against *S. aureus* and *E. coli* as depicted in Table 1. Statistically, significant inhibition areas ($p < 0.05$) for minimum and maximum concentrations of doped nanostructures, respectively against *Escherichia coli* (1.05–2.00 mm) and (1.35–2.25 mm) were attained. Broadly, zero activity was observed for TiO_2 and N-TiO_2 against *Staphylococcus aureus* at minimum and maximum concentrations while binary-doped samples showed substantial activity against *Escherichia coli* at both concentrations. Similarly, C_3N_4 depicted 1.60 mm inhibition area at maximum concentration only against *Escherichia coli*.

Anti-bacterial effectiveness is swayed by the scale of nanoparticles so oxidative stress of invented nanocomposites is dependent on scale and concentration [57]. An electrostatic contact between bacteria and nanoscale structures results in the generation of reactive oxygen species, which are lethal to cells [24, 58]. Oxygen reactive species (ROS) encircle bacteria external membrane and through extrusion and bulge of cytoplasmic components bacteria death occurs [59]. Micro pathogens ruin also proceeds when cations strongly bind with negative components of bacterial cells. Cations cause dysfunction in bacterial ribosomal activities and enzymatic degradation resulting collapse [60]. Two reactions have been identified as feasible for the bactericidal mechanism of nanomaterials, one of which involves strong interaction between the cations Ti^{+4} and bacterial cells, resulting in the formation of negativized sections and subsequent collapse, and the other of which involves electronic excitation of the TiO_2 valance band surface via irradiation. Additionally, the electrical O_2 reaction generates O^{-2} radicals, which results in the production of H_2O_2. The

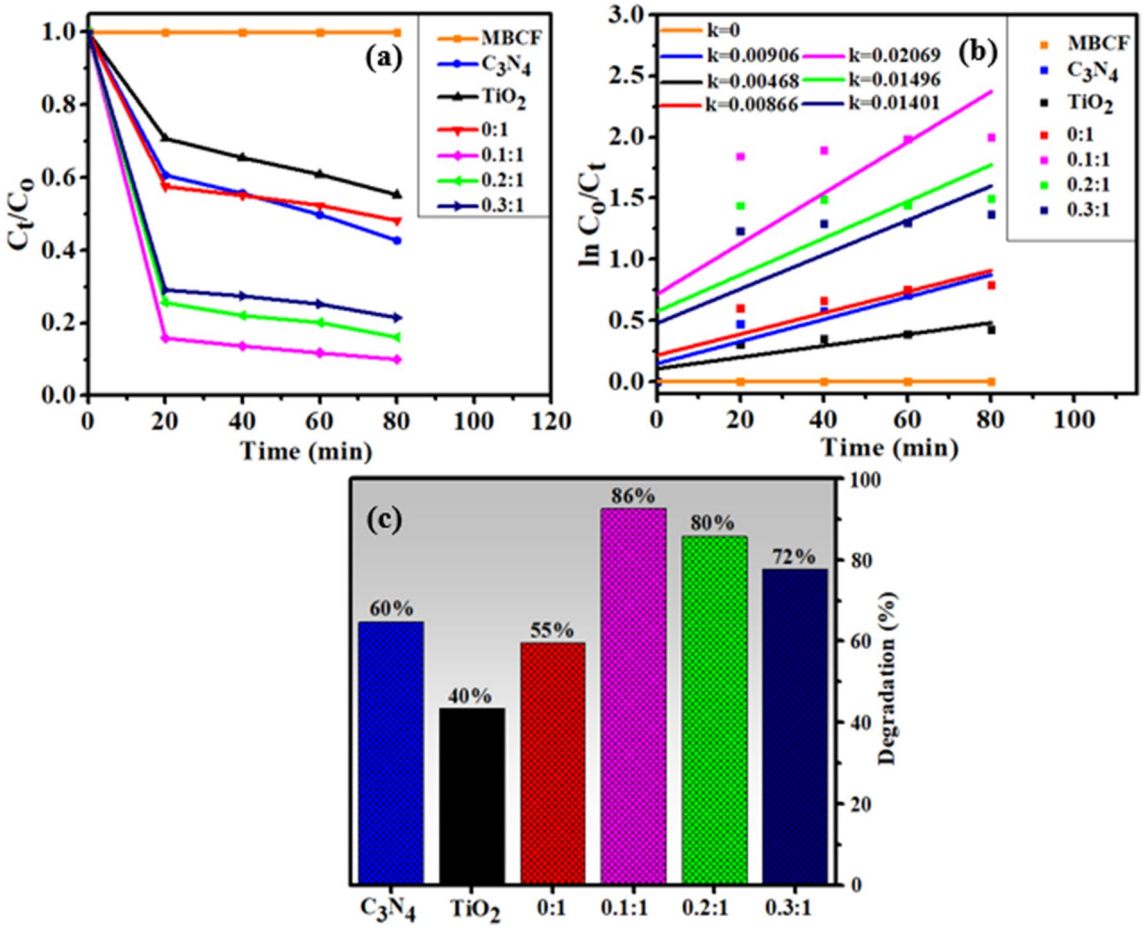

Fig. 9 **a** Plot of concentration ratio (C_t/C_o) versus time, **b** plot of ln(C_o/C_t) versus time spectra for dye reduction, **c** percentage (%) degradation of all prepared specimens

resultant O^{-2} species play a critical role in the breakdown of lipid or protein molecules on the bacteria's external cell membrane [61, 62].

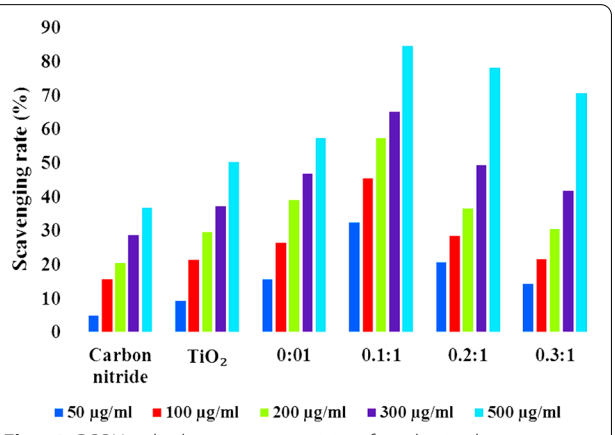

Fig. 10 DPPH radical scavenging activity of synthesized nanostructures

Conclusion

Binary-doped TiO_2 was synthesized through co-precipitation method and synthesized samples were evaluated for photo, sono and photo-sono catalytic degradation of MB and CF dyes and bactericidal activities. The strong contact formation between dopants and TiO_2 efficiently increased e^- to h^+ pairs separation efficiency induced by light. The narrow bandgap of C_3N_4:N/TiO_2 composite was accredited to N as well as C_3N_4 incorporation in pristine TiO_2. The prepared samples showed efficient degradation performance under visible light as well as under ultrasonic waves (SCA). Moreover, the combined effect of photo and sono catalysis was also evaluated for prepared catalysts for comparative study. Furthermore, prepared nanocomposites exhibited notable efficacy against *S. aureus* and *E. coli* bacteria as well. We believe that this study will open new insights into the fabrication of novel, binary doped heterojunctions for effective dye degradation and bactericidal applications in the future.

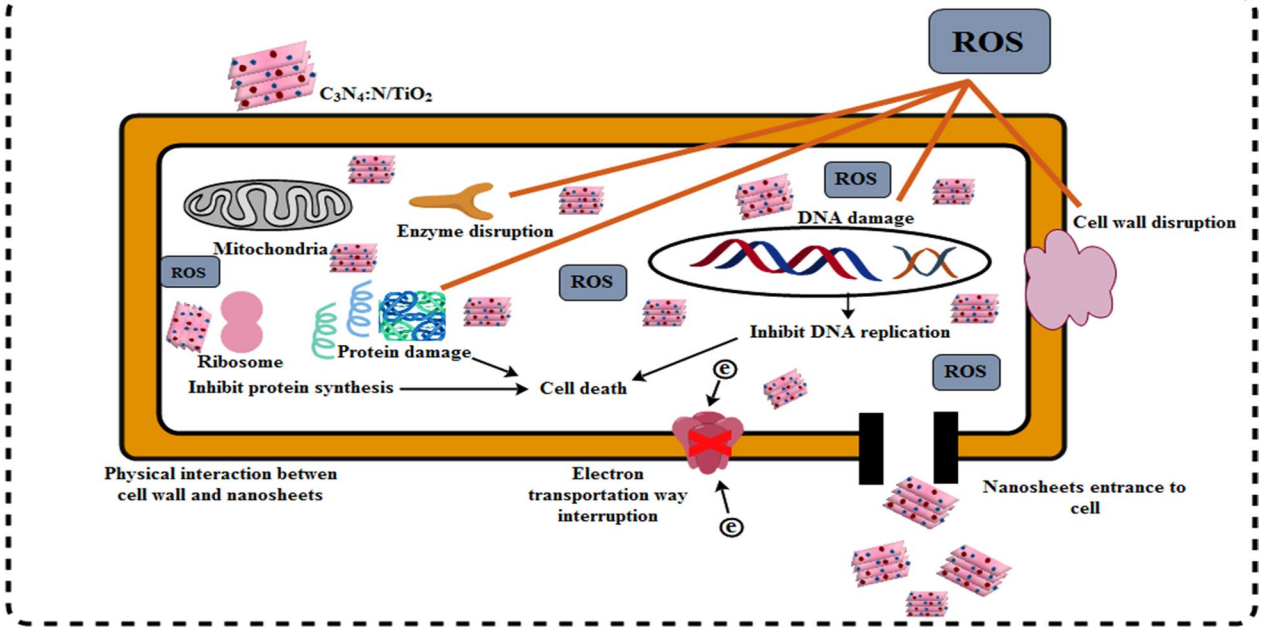

Fig. 11 Illustration of antimicrobial activity of prepared sample

Table 1 [a]Inhibition zone (mm) of binary-doped TiO_2 for *Staphylococcus aureus*. [b]Inhibition zone determination of binary-doped TiO_2 for *Escherichia coli*

	Inhibition zone[a]	(mm)	Inhibition zone[b]	(mm)
Sample	0.5 mg/50 µL	1.0 mg/50 µL	0.5 mg/50 µL	1.0 mg/50 µL
TiO_2	0	0	0	0
N-TiO_2	0	0	0	0
C_3N_4	0	0	0	1.60
0.1:1	0	0	1.05	1.35
0.2:1	0	0	1.50	2.05
0.3:1	0	0	2.0	2.25
Ciprofloxacin	4.45	4.45	4.25	4.25
DIW	0	0	0	0

Abbreviations

C_3N_4: Carbon nitride; EDS: Energy dispersive X-ray spectroscopy; FTIR: Fourier transform infrared spectroscopy; FESEM: Field emission scanning electron microscopy; G + ve: Gram-positive; G −ve: Gram negative; GO: Graphene; HR-TEM: High resolution transmission electron microscopy; JCPDS: Joint committee on powder diffraction standards; TiO_2: Titanium dioxide; UV–vis: Ultra-violet visible spectroscopy; XRD: X-ray diffraction.

Acknowledgements

Support provided by the Core Research Facilities at the King Fahd University of Petroleum & Minerals, Dhahran, Saudi Arabia is greatly appreciated.

Authors' contributions

AI and MI performed the whole experiments and AI wrote the manuscript. AH performed antimicrobial and participated in the data analysis of the results and discussion portion. JH and IS worked on schematic diagram and reviewed the manuscript, corrected the English. AUH carried out the FESEM and HRTEM analysis. All authors read and approved the final manuscript.

Funding

Authors are thankful to Higher Education Commission, HEC through start research grant project # 21-1669/SRGP/R&D/HEC/2017 Pakistan for financial support.

Availability of Data and Materials

All data are fully available without restriction.

Declarations

Conflict of interest

The authors declare that they have no conflict of interest.

Author details
[1]Solar Cell Application Research Lab, Department of Physics, Government College University Lahore, Lahore, Punjab 54000, Pakistan. [2]Department of Clinical Medicine and Surgery, University of Veterinary and Animal Sciences, Lahore, Punjab 54000, Pakistan. [3]Core Research Facilities, King Fahd University of Petroleum and Minerals, Dhahran 31261, Saudi Arabia. [4]Punjab University College of Pharmacy, University of the Punjab, Lahore 54000, Pakistan. [5]Tianjin Institute of Industrial Biotechnology, Chinese Academy of Sciences, Tianjin 300308, China.

Received: 6 April 2021 Accepted: 13 July 2021
Published online: 26 July 2021

References

1. Bettinelli M, Dallacasa V, Falcomer D, Fornasiero P, Gombac V, Montini T, Romanò L, Speghini A (2007) Photocatalytic activity of TiO2 doped with boron and vanadium. J Hazard Mater 146:529–534. https://doi.org/10.1016/j.jhazmat.2007.04.053
2. Zhang G, Song A, Duan Y, Zheng S (2018) Enhanced photocatalytic activity of TiO2/zeolite composite for abatement of pollutants. Microporous Mesoporous Mater 255:61–68. https://doi.org/10.1016/j.micromeso.2017.07.028
3. Miller RE, Shenoy VB (2000) Size-dependent elastic properties of nanosized structural elements. Nanotechnology 11:139–147. https://doi.org/10.1088/0957-4484/11/3/301
4. Lee JS, Jang J (2014) Hetero-structured semiconductor nanomaterials for photocatalytic applications. J Ind Eng Chem 20:363–371. https://doi.org/10.1016/j.jiec.2013.11.050
5. Manzoor M, Rafiq A, Ikram M, Nafees M, Ali S (2018) Structural, optical, and magnetic study of Ni-doped TiO2 nanoparticles synthesized by sol–gel method. Int Nano Lett 8:1–8. https://doi.org/10.1007/s40089-018-0225-7
6. Ikram M, Ali S, Murray R, Hussain A, Islahudin SIS (2015) Influence of fullerene derivative replacement with TiO2 nanoparticles in organic bulk heterojunction solar cells. Curr Appl Phys 15:48–54. https://doi.org/10.1016/j.cap.2014.10.026
7. Kang X, Liu S, Dai Z, He Y, Song X, Tan Z (2019) Titanium dioxide: from engineering to applications. Catalysts 9:191. https://doi.org/10.3390/catal9020191
8. Mathews NR, CortesJacome MA, Angeles-Chavez C, Toledo Antonio JA (2015) Fe doped TiO2 powder synthesized by sol gel method: structural and photocatalytic characterization. J Mater Sci Mater Electron 26:5574–5584. https://doi.org/10.1007/s10854-014-2294-3
9. Finegold L, Cude JL (1972) Biological sciences: One and two-dimensional structure of alpha-helix and beta-sheet forms of poly(L-Alanine) shown by specific heat measurements at low temperatures (15–20 K). Nature 238:38–40. https://doi.org/10.1038/238038a0
10. Bremner JM (1995) Recent research on problems in the use of urea as a nitrogen fertilizer. In: Nitrogen economic tropical soils, Springer, Netherlands, pp 321–329. https://doi.org/10.1007/978-94-009-1706-4_30
11. Marques J, Gomes TD, Forte MA, Silva RF, Tavares CJ (2019) A new route for the synthesis of highly-active N-doped TiO 2 nanoparticles for visible light photocatalysis using urea as nitrogen precursor. Catal Today 326:36–45. https://doi.org/10.1016/j.cattod.2018.09.002
12. Ansari SA, Khan MM, Ansari MO, Cho MH (2016) Nitrogen-doped titanium dioxide (N-doped TiO2) for visible light photocatalysis. New J Chem 40:3000–3009. https://doi.org/10.1039/c5nj03478g
13. Dunnill CW, Parkin IP (2011) Nitrogen-doped TiO2 thin films: Photocatalytic applications for healthcare environments. Dalt Trans 40:1635–1640. https://doi.org/10.1039/c0dt00494d
14. DiValentin C, Pacchioni G, Selloni A (2004) Origin of the different photoactivity of N-doped anatase and rutile TiO2. Phys Rev B Condens Matter Mater Phys. https://doi.org/10.1103/PhysRevB.70.085116
15. Yang Y, Mao B, Gong G, Li D, Liu Y, Cao W, Xing L, Zeng J, Shi W, Yuan S (2019) In-situ growth of Zn–AgIn5S8 quantum dots on g-C3N4 towards 0D/2D heterostructured photocatalysts with enhanced hydrogen production. Int J Hydrogen Energy 44:15882–15891. https://doi.org/10.1016/j.ijhydene.2019.01.102
16. Abebe B, Murthy HCA, Amare E (2020) Enhancing the photocatalytic efficiency of ZnO: defects, heterojunction, and optimization. Environ Nanotechnol Monit Manag 14:100336. https://doi.org/10.1016/j.enmm.2020.100336
17. Zhang X, Yuan X, Jiang L, Zhang J, Yu H, Wang H, Zeng G (2020) Powerful combination of 2D g-C3N4 and 2D nanomaterials for photocatalysis: recent advances. Chem Eng J 390:124475. https://doi.org/10.1016/j.cej.2020.124475
18. Abebe B, Zereffa EA, Murthy HCA (2021) Synthesis of poly(vinyl alcohol)-aided ZnO/Mn2O3 nanocomposites for acid orange-8 dye degradation: mechanism and antibacterial activity. ACS Omega 6:954–964. https://doi.org/10.1021/acsomega.0c05597
19. Maness PC, Smolinski S, Blake DM, Huang Z, Wolfrum EJ, Jacoby WA (1999) Bactericidal activity of photocatalytic TiO2 reaction: toward an understanding of its killing mechanism. Appl Environ Microbiol 65:4094–4098. https://doi.org/10.1128/aem.65.9.4094-4098.1999
20. Abebe B, Murthy HCA, Zereffa EA (2021) Nano commentary multifunctional application of PVA-aided Zn-Fe-Mn coupled oxide nanocomposite. Nanoscale Res Lett 16:1. https://doi.org/10.1186/s11671-020-03464-0
21. Abebe B, Zereffa EA, Tadesse A, Murthy HCA (2020) A review on enhancing the antibacterial activity of ZnO: mechanisms and microscopic investigation. Nanoscale Res Lett 15:1–19. https://doi.org/10.1186/s11671-020-03418-6
22. Altaf S, Ajaz H, Imran M, Ul-Hamid A, Naz M, Aqeel M, Shahzadi A, Shahbaz A, Ikram M (2020) Synthesis and characterization of binary selenides of transition metals to investigate its photocatalytic, antimicrobial and anticancer efficacy. Appl Nanosci 10:2113–2127. https://doi.org/10.1007/s13204-020-01350-w
23. Kibiti CM, Afolayan AJ (2015) Preliminary phytochemical screening and biological activities of *Bulbine abyssinica* used in the folk medicine in the Eastern Cape Province, South Africa. Evid Based Complem Altern Med. https://doi.org/10.1155/2015/617607
24. Haider A, Ijaz M, Imran M, Naz M, Majeed H, Khan JA, Ali MM, Ikram M (2020) Enhanced bactericidal action and dye degradation of spicy roots' extract-incorporated fine-tuned metal oxide nanoparticles. Appl Nanosci 10:1095–1104. https://doi.org/10.1007/s13204-019-01188-x
25. Zhang H, Liu F, Wu H, Cao X, Sun J, Lei W (2017) In situ synthesis of g-C3N4/TiO2 heterostructures with enhanced photocatalytic hydrogen evolution under visible light. RSC Adv 7:40327–40333. https://doi.org/10.1039/c7ra06786k
26. Ikram M, Umar E, Raza A, Haider A, Naz S, Ul-Hamid A, Haider J, Shahzadi I, Hassan J, Ali S (2020) Dye degradation performance, bactericidal behavior and molecular docking analysis of Cu-doped TiO2nanoparticles. RSC Adv 10:24215–24233. https://doi.org/10.1039/d0ra04851h
27. Rajamannan B, Mugundan S, Viruthagiri G, Praveen P, Shanmugam N (2014) Linear and nonlinear optical studies of bare and copper doped TiO2 nanoparticles via sol gel technique. Spectrochim Acta Part A Mol Biomol Spectrosc 118:651–656. https://doi.org/10.1016/j.saa.2013.09.045
28. Ansari ZA, Umar A, Fouad H, Ansari SG (2015) Dye sensitized solar cells fabricated using Cu-Doped TiO2 nanopowder with anthocyanin as sensitizer. J Nanoelectron Optoelectron 10:290–294. https://doi.org/10.1166/jno.2015.1749
29. Álvaro RJ, Diana ND, MorantesMaría A (2017) Effect of Cu on optical properties of TiO2 nanoparticles. Contemp Eng Sci 10:1539. https://doi.org/10.12988/ces.2017.711182
30. Han C, Wang Y, Lei Y, Wang B, Wu N, Shi Q, Li Q (2015) In situ synthesis of graphitic-C3N4 nanosheet hybridized N-doped TiO2 nanofibers for efficient photocatalytic H2 production and degradation. Nano Res 8:1199–1209. https://doi.org/10.1007/s12274-014-0600-2
31. Song X, Hu Y, Zheng M, Wei C (2016) Solvent-free in situ synthesis of g-C3N4/{001}TiO2 composite with enhanced UV- and visible-light photocatalytic activity for NO oxidation. Appl Catal B Environ 182:587–597. https://doi.org/10.1016/j.apcatb.2015.10.007
32. Liu C, Huang H, Du X, Zhang T, Tian N, Guo Y, Zhang Y (2015) In situ co-crystallization for fabrication of g-C3N4/Bi5O7I heterojunction for enhanced visible-light photocatalysis. J Phys Chem C 119:17156–17165. https://doi.org/10.1021/acs.jpcc.5b03707
33. Tan S, Xing Z, Zhang J, Li Z, Wu X, Cui J, Kuang J, Yin J, Zhou W (2017) Meso-g-C3N4/g-C3N4 nanosheets laminated homojunctions as efficient visible-light-driven photocatalysts. Int J Hydrogen Energy 42:25969–25979. https://doi.org/10.1016/j.ijhydene.2017.08.202

34. Kong HJ, Won DH, Kim J, Woo SI (2016) Sulfur-doped g-C3N4/BiVO4 composite photocatalyst for water oxidation under visible light. Chem Mater 28:1318–1324. https://doi.org/10.1021/acs.chemmater.5b04178
35. Wang Y, Rao L, Wang P, Shi Z, Zhang L (2020) Photocatalytic activity of N-TiO2/O-doped N vacancy g-C3N4 and the intermediates toxicity evaluation under tetracycline hydrochloride and Cr(VI) coexistence environment. Appl Catal B Environ 262:118308. https://doi.org/10.1016/j.apcatb.2019.118308
36. Le P, Hieu L, Lam T-N, Hang N, Truong N, Tuyen L, Phong P, Leu J (2018) Enhanced photocatalytic performance of nitrogen-doped TiO2 nanotube arrays using a simple annealing process. Micromachines 9:618. https://doi.org/10.3390/mi9120618
37. Raja V, JaffarAli BM (2021) Synergy of photon up-conversion and Z-scheme mechanism in graphitic carbon nitride nanoparticles decorated g-C3N4-TiO2. Colloids Surf A Physicochem Eng Asp 611:125862. https://doi.org/10.1016/j.colsurfa.2020.125862
38. Chen Z, Fan T, Shao M, Yu X, Wu Q, Li J, Fang W, Yi X (2019) Simultaneously enhanced photon absorption and charge transport on a distorted graphitic carbon nitride toward visible light photocatalytic activity. Appl Catal B Environ 242:40–50. https://doi.org/10.1016/j.apcatb.2018.09.080
39. Abebe B, Murthy HCA, Zereffa EA (2020) Synthesis and characterization of PVA-assisted metal oxide nanomaterials: surface area, porosity, and electrochemical property improvement. J Nanomater. https://doi.org/10.1155/2020/6532835
40. Li P, Zhang X, Qiu L, Xu X, Si Y, Liang T, Liu H, Chu J, Guo J, Duo S (2020) MOF-derived TiO2modified with g-C3N4nanosheets for enhanced visible-light photocatalytic performance. New J Chem 44:6958–6964. https://doi.org/10.1039/d0nj00746c
41. Shockley W, Read WT (1952) Statistics of the recombinations of holes and electrons. Phys Rev 87:835–842. https://doi.org/10.1103/PhysRev.87.835
42. Cushing SK, Meng F, Zhang J, Ding B, Chen CK, Chen CJ, Liu RS, Bristow AD, Bright J, Zheng P, Wu N (2017) Effects of defects on photocatalytic activity of hydrogen-treated titanium oxide nanobelts. ACS Catal 7:1742–1748. https://doi.org/10.1021/acscatal.6b02177
43. Gurlo A (2006) Interplay between O2 and SnO2: oxygen ionosorption and spectroscopic evidence for adsorbed oxygen. ChemPhysChem 7:2041–2052. https://doi.org/10.1002/cphc.200600292
44. Ajmal A, Majeed I, Malik RN, Idriss H, Nadeem MA (2014) Principles and mechanisms of photocatalytic dye degradation on TiO 2 based photocatalysts: a comparative overview. RSC Adv 4:37003–37026. https://doi.org/10.1039/c4ra06658h
45. Pang X, Chen C, Ji H, Che Y, Ma W, Zhao J (2014) Unraveling the photocatalytic mechanisms on TiO2 surfaces using the oxygen-18 isotopic label technique. Molecules 19:16291–16311. https://doi.org/10.3390/molecules191016291
46. Yu J, Park J, Van Wyk A, Rumbles G, Deria P (2018) Excited-state electronic properties in Zr-based metal-organic frameworks as a function of a topological network. J Am Chem Soc 140:10488–10496. https://doi.org/10.1021/jacs.8b04980
47. Younis SA, Kwon EE, Qasim M, Kim KH, Kim T, Kukkar D, Dou X, Ali I (2020) Metal-organic framework as a photocatalyst: progress in modulation strategies and environmental/energy applications. Prog Energy Combust Sci 81:100870. https://doi.org/10.1016/j.pecs.2020.100870
48. Dhakshinamoorthy A, Li Z, Garcia H (2018) Catalysis and photocatalysis by metal organic frameworks. Chem Soc Rev 47:8134–8172. https://doi.org/10.1039/c8cs00256h
49. Wang J, Jiang Z, Zhang Z, Xie Y, Lv Y, Li J, Deng Y, Zhang X (2009) Study on inorganic oxidants assisted sonocatalytic degradation of Acid Red B in presence of nano-sized ZnO powder. Sep Purif Technol 67:38–43. https://doi.org/10.1016/j.seppur.2009.03.005
50. Xin Ying G, Tunku Abdul Rahman U (2018) Synthesis of TiO2/G-C3N4 composite for sonocatalytic degradation of organic dye
51. Isono R, Yoshimura T, Esumi K (2005) Preparation of Au/TiO2 nanocomposites and their catalytic activity for DPPH radical scavenging reaction. J Colloid Interface Sci 288:177–183. https://doi.org/10.1016/j.jcis.2005.02.078
52. Morsella M, D'Alessandro N, Lanterna AE, Scaiano JC (2016) Improving the sunscreen properties of TiO2 through an understanding of its catalytic properties. ACS Omega 1:464–469. https://doi.org/10.1021/acsomega.6b00177
53. Huang CW, Wu MC (2020) Photocatalytic degradation of methylene blue by UV-assistant TiO2 and natural sericite composites. J Chem Technol Biotechnol 95:2715–2722. https://doi.org/10.1002/jctb.6392
54. Su J, Zhu L, Geng P, Chen G (2016) Self-assembly graphitic carbon nitride quantum dots anchored on TiO2 nanotube arrays: an efficient heterojunction for pollutants degradation under solar light. J Hazard Mater 316:159–168. https://doi.org/10.1016/j.jhazmat.2016.05.004
55. Javed R, Ahmed M, UlHaq I, Nisa S, Zia M (2017) PVP and PEG doped CuO nanoparticles are more biologically active: antibacterial, antioxidant, antidiabetic and cytotoxic perspective. Mater Sci Eng C 79(2017):108–115. https://doi.org/10.1016/j.msec.2017.05.006
56. Javed R, Usman M, Tabassum S, Zia M (2016) Effect of capping agents: structural, optical and biological properties of ZnO nanoparticles. Appl Surf Sci 386:319–326. https://doi.org/10.1016/j.apsusc.2016.06.042
57. Ahmed B, Solanki B, Zaidi A, Khan MS, Musarrat J (2019) Bacterial toxicity of biomimetic green zinc oxide nanoantibiotic: insights into ZnONP uptake and nanocolloid–bacteria interface. Toxicol Res (Camb) 8:246–261. https://doi.org/10.1039/C8TX00267C
58. Ahmed B, Hashmi A, Khan MS, Musarrat J (2018) ROS mediated destruction of cell membrane, growth and biofilms of human bacterial pathogens by stable metallic AgNPs functionalized from bell pepper extract and quercetin. Adv Powder Technol 29:1601–1616. https://doi.org/10.1016/j.apt.2018.03.025
59. Ikram M, Tabassum R, Qumar U, Ali S, Ul-Hamid A, Haider A, Raza A, Imran M, Ali S (2020) Promising performance of chemically exfoliated Zr-doped MoS2nanosheets for catalytic and antibacterial applications. RSC Adv 10:20559–20571. https://doi.org/10.1039/d0ra02458a
60. Altaf S, Haider A, Naz S, Ul-Hamid A, Haider J, Imran M, Shahzadi A, Naz M, Ajaz H, Ikram M (2020) Comparative study of selenides and tellurides of transition metals (Nb and Ta) with respect to its catalytic, antimicrobial, and molecular docking performance. Nanoscale Res Lett 15:1–16. https://doi.org/10.1186/s11671-020-03375-0
61. Haider A, Ijaz M, Ali S, Haider J, Imran M, Majeed H, Shahzadi I, Ali MM, Khan JA, Ikram M (2020) Green synthesized phytochemically (*Zingiber officinale* and *Allium sativum*) reduced nickel oxide nanoparticles confirmed bactericidal and catalytic potential. Nanoscale Res Lett 15:1–11. https://doi.org/10.1186/s11671-020-3283-5
62. Iyyappa Rajan P, Judith Vijaya J, Jesudoss SK, Kaviyarasu K, John Kennedy L, Jothiramalingam R, Al-Lohedan HA, Vaali-Mohammed MA (2017) Green-fuel-mediated synthesis of self-assembled NiO nano-sticks for dual applications-photocatalytic activity on Rose Bengal dye and antimicrobial action on bacterial strains. Mater Res Express 4:85030. https://doi.org/10.1088/2053-1591/aa7e3c

Publisher's Note